

pubs.acs.org/Macromolecules Article

Hierarchical Self-Assembly of Poly(D-glucose carbonate) Amphiphilic **Block Copolymers in Mixed Solvents**

Jee Young Lee, Yue Song, Michiel G. Wessels, Arthi Jayaraman,* Karen L. Wooley,* and Darrin J. Pochan*



Cite This: https://dx.doi.org/10.1021/acs.macromol.0c01575



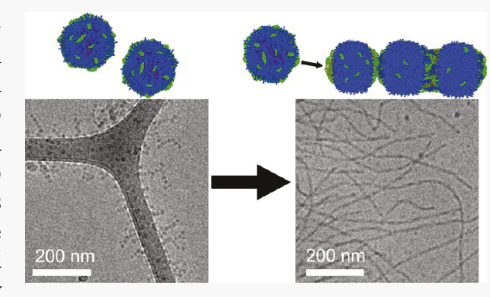
ACCESS I

Metrics & More

Article Recommendations

Supporting Information

ABSTRACT: We report the fibril formation of poly(D-glucose carbonate) (PGC)based amphiphilic diblock copolymers using solution assembly. Unlike conventional cylindrical micelles constructed from amphiphilic block copolymers (BCPs) with coil-like blocks, the assembled PGC fibrils exhibit thin, ribbon-like features due to significant stiffness and hydrophobicity of the PGC BCP backbone that result in a unique polymer chain packing. A tetrahydrofuran/H₂O solvent mixture was used to create a solvent quality gradient during which a hierarchical assembly pathway was observed with fibril precursor nanoparticles that linked together into fibrils. These initial precursors were soft, patchy nanoparticles caused by the phase-segregated hydrophilic block of the PGC diblock copolymer. With aging, the patchy



nanoparticles underwent unidirectional attachment through hydrophobic association to transform into uniform fibril structures. Transmission electron microscopy, interpretation of the small-angle neutron scattering measurements fit with analytical models, and genetic algorithm-based reverse engineering of structure confirmed the presence of initial particle precursors, intermediate stages during growth, and the fully matured fibrils. The results suggest that unconventional backbone chemistry-based molecules reveal unique effects of chain stiffness and hydrophobicity on block copolymer solution assembly when using glucose-based polycarbonates.

1. INTRODUCTION

In solution, amphiphilic molecules are known for their ability to self-organize into well-defined morphologies including micellar, vesicular, or mixed/hybrid structures, each of which is interesting for the ability to access complex nanoscopic dimensions, geometries, and properties. Specifically, one can take advantage of slow chain kinetics of BCP chains in specific solvent conditions and their inability to reach global equilibrium to form nanostructures that exhibit enhanced robustness and diversity compared to those available by the assembly of small molecule amphiphiles. Advances in solution processing methods have been explored with complex interplay of assembly variables, including molecular designs (e.g., polymer compositions^{2–4} and monomer chemistry^{5,6}), solvent conditions (e.g., choice of solvent or solvent mixtures, temperature, and small-molecule addition, and different kinetic pathways (e.g., crystallization-driven, solvent titration, emulsification, and polymerization-induced). These parameters give rise to specific interfacial curvature between the core and corona where a balance of chain block conformation and the interfacial tension at their interface, both impacted by selective solvent swelling of the solvophobic and solvophilic domains, create the unique aggregate characteristics in response to specific assembly pathways. In most of the coilcoil block copolymers, the particular chain conformation and packing in the formed aggregates are possible due to the flexible nature of the BCP coil backbone that allows the chains

to collapse or expand to a preferred conformation without significant resistance to bending. However, many naturally occurring polymers, such as DNA or polysaccharides, exhibit inherent chain stiffness, where the chain conformation in an unfavorable solvent condition is largely determined by the chain rigidity and large persistence length. This chain stiffness is especially significant for charged polymers or polymers with bulky monomers. 16,17 When the backbones of BCPs exhibit substantial rigidity, the assembly behavior is expected to exhibit a different behavior from coil-based BCPs, especially if the solvent environment is incompatible with the backbone chemistry.18

The effects of polymer backbone stiffness and hydrophobicity on BCP chain packing in an assembled nanostructure have important implications due to efforts to organize various biopolymers in confinement to be used for applications such as gene or drug delivery carriers. Semiflexible polymers in an unfavorable solution condition are known to produce torus particles, 22,23 spindles, 24,25 hollow spheres, 6 or disk-like^{27,28} collapsed structures depending on the polymer

Received: July 8, 2020 Revised: September 1, 2020



Macromolecules Article pubs.acs.org/Macromolecules

chain bending stiffness and polymer length. 28,29 While both experimental and simulation studies have demonstrated a coilglobule transition using homopolymer DNA^{24,25,30} or various modified polysaccharide molecules, 31,32 little has been reported on the hierarchical organization of collapsed BCP chains with stiff backbone chemistry into well-defined nanostructures. Bates, Lodge, Larson, and coworkers reported robust fibril formation of semiflexible methylcellulose, for which the chains were hypothesized to form a toroidal configuration at an elevated temperature that subsequently packed unidirectionally to form fibrils. 33,34 Similarly, Liu and coworkers have shown that ethyl cellulose-based graft copolymers with different side chain lengths were able to be controllably collapsed in different solvent mixtures to form necklace-like networks. 35,36 Furthermore, the self-assembly behavior of rod-coil BCP systems containing stiff polymer blocks^{37,38} (e.g., conjugated polyor polypeptide-based molecules with helical secondary structure (42-44) is dominated by the orientational ordering of the rigid polymer chains 45,46 that leads to formation of non-conventional BCP nanostructures, including tubules 43 or ribbons. 40,41 These examples demonstrate the possible complexity in assembly pathways and final assembled structures observed with semiflexible, stiff backbone polymers while also presenting challenges for a better understanding of chain packing mechanisms and opportunities to take advantage of stiff chain conformations during solution assembly.

In the work presented here, we use a poly(D-glucose carbonate) (PGC)-based amphiphilic diblock copolymer system where the entire backbone is composed of a semiflexible, sugar-based PGC, and amphiphilicity between blocks is created by the incorporation of a different side chain chemistry within distinct block regions. With a solvent titration method, the PGC BCPs are assembled into ribbon-like fibrils with features that do not follow traditional cylindrical micellelike chain packing. The fibril formation is achieved hierarchically where precursor nanoparticles are first formed upon the addition of water to an organic BCP solution with subsequent interparticle associations occurring through hydrophobic patches. Interparticle association driving hierarchical assembly has been reported for soft, patchy micelles where micelle/ particle corona patches link together by either ion binding 47,48 or through hydrophobic association of chemically distinctive domains. 49,50 In our system, we hypothesize that the patchiness is a result of the PGC backbone segregating from hydrophilic side chains on the exterior of the nanoparticles, similar to collapsed conformations and observed aggregates of grafted bottlebrush polymers with different backbones and side chain solubilities in a selective solvent. 35,51,52 We show that while the rigidity of the PGC backbone influences the local BCP chain conformation and packing in the formed nanostructure, the backbone hydrophobicity drives 1D fibril growth by forming sticky domains on the exterior of the initially formed nanoparticles. Cryogenic transmission electron microscopy (cryo-TEM), small-angle neutron scattering (SANS), and computational reverse engineering of the scattering experiments (CREASE)⁵³ confirm the PGC final fibril structure and the intermediate stages during the fibril formation, which are captured due to relatively slow fibril growth. These results suggest that the stiffness and hydrophobicity of semiflexible backbone monomeric repeat units are important factors that determine the assembly pathway and final morphology of glucose carbonate-based BCP solution assembly.

2. METHODS

2.1. Synthesis of Side Chain-Modified PGC Block Copoly**mers.** The poly(methyl-2,3-O-ethoxycarbonyl-4,6-O-carbonyl- α -Dglucopyranoside)-b-poly(methyl-2-O-ethoxycarbonyl-3-O-propargyloxycarbonyl-4,6-O-carbonyl- α -D-glucopyranoside) [PGC(EEC)₉₈-b-PGC(EPC)₃₀] diblock copolymer was synthesized by one-pot sequential organocatalyzed ring-opening polymerization (ROP) with a monomer feed ratio [GC-(EEC)]/[GC(EPC)] of 3:1 to ensure a specific block composition. The cationic side chain modification was then done by post-polymerization modification of PGC(EEC)₉₈-b-PGC(EPC)₃₀ using a photoinitiated thiol-yne click reaction with cysteamine hydrochloride to afford PGC(EEC)₉₈-b-PGC(EPC)-(NH₃Cl)₃₀. Detailed synthetic methods are described elsewhere. Characterization of the diblock copolymer PGC(EEC)₉₈-b-PGC-(EPC)₃₀ and post-polymerized cationic modified polymer PGC-(EEC)₉₈-b-PGC(EPC)(NH₃Cl)₃₀ was reported in a previous study. The specific chemical structure of the PGC(EEC)₉₈-b-PGC(EPC)- $(NH_3Cl)_{30}$ diblock copolymer is provided in Figure 1.

Figure 1. Chemical structure of the poly(D-glucose carbonate) block copolymer with the PGC backbone illustrated in green, the hydrophobic side chains in red, and hydrophilic side chains in blue.

2.2. Fibril Assembly Pathway. The amphiphilic PGC BCPs were first dissolved in an organic solvent, tetrahydrofuran (THF). Then, pure Milli-Q water was slowly titrated dropwise to the polymersolvent mixture at a rate of 1 mL/h until the water volume reached 40 vol % at a final polymer concentration ranging from 0.04 to 0.4 wt %. The samples were then aged for different amounts of time (no aging up to two weeks of aging) to observe fibril formation progress. During the aging, samples were stored in PTFE-lined glass vials and sealed with PTFE tape and a parafilm to eliminate solvent evaporation. The solution level was constantly checked throughout the aging to verify a constant THF/H₂O volume ratio. For SANS sample preparation, d₈-THF and D₂O were used to provide scattering contrast between the assembled nanostructure and the solvent mixture. The BCP concentration range used for these experiments did not affect the final assembly morphologies.

2.3. Characterization. 2.3.1. Transmission Electron Microscopy (TEM). TEM imaging was performed on a FEI TALOS with a Falcon II direct electron detector camera at an electron accelerating voltage of 200 keV. Cast film TEM grids were prepared by applying 3 μ L of the sample onto a plasma-cleaned carbon-coated copper grid purchased from Electron Microscopy Sciences. All cast film samples were negatively stained with sodium phosphotungstic acid (PTA) (2 wt %, pH 7). The staining solution was directly introduced to the grid right after the sample solution was blotted away. The remaining staining solution was then wicked away with a filter paper.

Cryogenic TEM (cryo-TEM) vitrified grid preparation was done using the Vitrobot, an automated plunge device that vitrifies a thin layer of desired solution. Depending on the sample concentration, the blotting parameters can be adjusted. Here, blotting was varied between 2 and 3 applications with a blotting time of 1-2 s at 100% humidity. The sample grids were rested for 1-2 s post-blotting. For preparing the vitrified THF sample, the humidity was set lower, and the chamber was saturated with THF to ensure no solvent composition change during the blotting process. To achieve an extremely fast cooling rate (~106 °C/s) for a homogeneous vitreous layer, the grid was first plunged into liquid ethane (90 K) and then

transferred and stored in $\rm LN_2$ until imaging. During the imaging, the cryo-TEM holder (Gatan 626 single tilt cryo-holder) was maintained at $-177~^{\circ}\rm C$ to prevent solvent crystallization. Lacey carbon grids from Ted Pella, Inc. were used for all grid preparations. All images were analyzed using Fiji-ImageJ software so with at least 50 width measurements both along the same fibril and within different fibrils to ensure a global representation of the assembled structure.

2.3.2. Small-Angle Neutron Scattering (SANS). SANS experiments were conducted using an NGB-7 30m SANS at the Center for Neutron Research (NCNR), a part of the National Institute for Standards and Technology (NIST, Gaithersburg, MD). The standard configuration at 1, 4, and 13 m sample-to-detector distances was used to collect data at a q-range of 0.003 to 0.5 $\mbox{\AA}^{-1}$ where q is the scattering vector; $q = \left(\frac{4\pi}{\lambda}\right) \sin\left(\frac{\theta}{\lambda}\right)$ with $\lambda = 6$ Å as an incident wavelength and θ as the scattering angle. Titanium sample cells with 1 mm thickness were mounted on a rotating cell holder to prevent sample sedimentation during the measurement. Before loading, all samples were degassed to remove air bubbles, and all experiments were carried out at an ambient condition. All collected data were corrected for the instrumental background, empty cell scattering, and detector efficiency, as well as radially averaged to 1D data and normalized to an absolute scale in units of cm⁻¹ based on the NIST NCNR data reduction protocol. SANS data were fitted with models available in SasView software⁵⁷ including the parallelepiped, elliptical cylinder, and flexible elliptical cylinder model. All models describe a long 1D structure with fitting parameters characterizing the width, height, and the Kuhn length in the case of the flexible elliptical cylinder model, but the models have different cross-sectional geometries: a rectangular geometry for the parallelepiped model and an ellipse for the elliptical models. The Schultz distribution (number-average) available in SasView was also used to account for the polydispersity of the fibril width and height.

2.3.3. Computational Reverse Engineering of Scattering Experiments (CREASE). For structural interpretation of the SANS intensity profiles without the models in SasView, a computational reverse engineering approach (CREASE)⁵³ was used. Specifically, the genetic algorithm (GA) portion of the CREASE method was used to calculate the dimensions for a variety of potential shapes of the assembled structure formed from the PGC amphiphilic BCPs. The overview of the GA is shown in Figure S1. The input to the GA included the scattering intensity profiles from experiments ($I_{exp}(q)$ versus q), the BCP design, and the hypothesized shape of the BCP assembled structure (e.g., spherical, cylinder, and parallelepiped). BCP design information included the chemistry of the BCP (i.e., the solvophilic block PGC(EEC) referred to as A (for brevity) and the solvophobic block PGC(EPC)(NH₃Cl) referred to as B), the BCP sequence (diblock), the number of repeat units in the solvophilic block (N_A = 30) and solvophobic block ($N_{\rm B}$ = 98), the molar mass of each repeat unit ($M_A = 601$ g/mol and $M_B = 364$ g/mol), the contour lengths of each repeat unit ($l_{\text{mono,A}} = 0.72 \text{ nm}$ and $l_{\text{mono,B}} = 0.72 \text{ nm}$), and the density of the solvophobic block, ($\rho_P = 1.13 \text{ g/mL}$), taken as the bulk density of the solvophobic polymer chemistry at the same temperature and pressure as the assembly conditions. The assembled structure shapes tested with GA were cylinders (with/without coronas), parallelepipeds (without coronas/with corona of equal width in all directions and independent width on the side and top of the parallelepipeds), and elliptical cylinders (with/without coronas). For a given input, the GA method outputs the dimensions of the BCP assembled structure (e.g., diameter and length of cylinders, core and corona sizes for cylinders or parallelepiped) whose computational scattering intensity profile best matches the input experimental scattering profiles.

A comprehensive description of the GA implementation is provided in our recent publication. ⁵³ The key details of the GA method that are pertinent to this study are described next. The reader is directed to the Supporting Information (section 1.2) for other details. Briefly, for each proposed assembly shape, the GA started with a random population consisting of 80 different individuals with different micelle dimensions. The number of individuals within a

population was chosen based on values that can minimize the computational intensity and maximize genetic diversity (i.e., explore a large number of possible solutions). For each individual in a generation, point scatterers with a diameter of 7.7 nm were randomly placed within the dimensions (e.g., width and height) of the input shape. The justification for the number and size of point scatters is provided in the Supporting Information. Using the point scatterer positions, the computational scattering intensity $I_{\rm comp}(q)$ was calculated (see Supporting Information section 1.2 for the details of this step). For each $I_{\rm comp}(q)$, the sum of (log difference) squared errors, sse, was calculated with eq 1

$$sse = \sum w[\log(I_{exp}(q)/I_{comp}(q))]^{2}$$
(1)

with the weight w being proportional to $\log(\Delta q)$. The fitness of each individual in the generation was calculated by comparing the $I_{\rm comp}(q)$ and the $I_{\rm exp}(q)$ using eq 2; a high value of the fitness indicates a close match between the $I_{\rm comp}(q)$ and the $I_{\rm exp}(q)$. To define the fitness, the sum of squared errors (sse) is rescaled as

$$Fitness = X(sse_{max} - sse) + Y$$
 (2)

where $\ensuremath{\mathsf{sse}}_{max}$ is the maximum sse for an individual of the current population, and the parameters X and Y serve to ensure that the GA does not converge prematurely.⁵³ Through a ranking that is proportional to the individuals' fitness values, the individuals with high fitness were selected for the next generation. Besides retaining the best fitting individual as is for the next generation, some selected individuals then went through a "crossover" or "mutation", mechanisms used in the GA to bring some diversity and improve matching of $I_{\text{comp}}(q)$ and the $I_{\text{exp}}(q)$ over multiple generations. For these next generations of individuals, the same steps of calculating fitness, selection, crossover, and mutation were repeated. This procedure was iterated for 100 generations, after which the best and average fitness values plateaued for at least five consecutive generations. The dimensions of the individual with the highest fitness were saved for the GA run as the "best" structure whose $I_{comp}(q)$ matches the $I_{exp}(q)$. Ten such trials or runs of the GA were conducted for each input to determine the variability in the "best" structures. We report the average and standard error for the structural dimensions calculated from the "best" structures of these 10 trials.

3. RESULTS AND DISCUSSION

Dilute solution assemblies of PGC amphiphilic BCPs were formed in mixed THF/water (60/40 v/v %). Representative TEM images of the BCP fibril structure are presented in Figure 2A,B. When fully matured, the PGC BCPs formed μ m long fibrils with a width of 13.2 \pm 0.3 nm measured from cryo-TEM images. The arrows in Figure 2C show structural details, such as twists and folds, which indicate that these fibrils resemble thin ribbon-like structures rather than a conventional cylindrical micelle seen from coil-based BCPs assembled in a similar assembly method. ^{12,58} Local density fluctuations within the fibrils from the cryo-TEM image in Figure 2A highlighted with black arrows also confirm the presence of twists, suggesting that the fibril cross section resembles a thin elliptical or rectangular geometry rather than a cylinder.

Complete fibril formation after sample preparation required a few days of aging, allowing one to observe initial, intermediate, and final stages of fibril growth. Starting from PGCs in pure THF organic solution in Figure S3, the initial nanostructure is best described as inverse micelle-like aggregates with ionic hydrophilic blocks primarily in the particle cores and hydrophobic blocks forming the particle shells due to THF being a poor solvent for the ionic side chains and a good solvent for the backbone and the hydrophobic block. Subsequent water titration, which

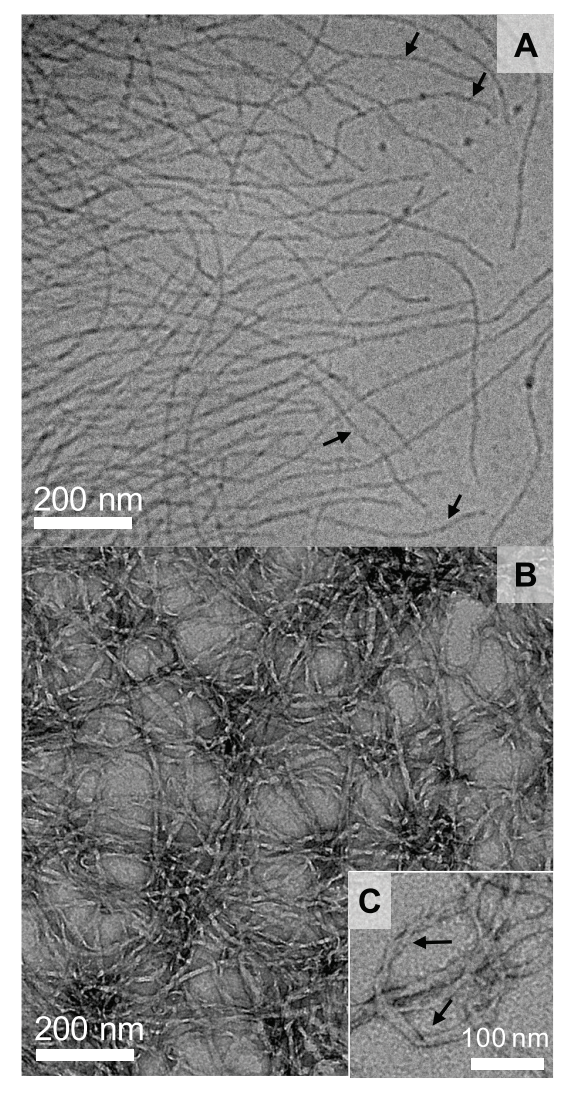


Figure 2. (A) Cryogenic-TEM image showing the fibril structures with an average fibril width of 13.2 nm. Arrows in A show twist regions with a different density contrast along the fibril. (B) Negatively stained TEM image is provided to show more detailed characteristics such as (C) folds and twists that are hard to observe from cryo-TEM due to a low contrast from solvent swollen nanostructures. Both images are from the same sample concentration of 0.4 wt %.

introduced a selective solvent for the hydrophilic side chains, induced a local chain rearrangement. The rearrangement is likely to start with the display of the hydrophilic side chains as the coronal moieties, while the hydrophobic association drives the shielding of the hydrophobic moieties in the core and the collapsing of the PGC backbone. This type of hydrophilichydrophobic block inversion from an inverse aggregate has been proposed from previous BCP assembly studies using the solvent titration method where the addition of a solvophilic block-selective solvent initiated the chain rearrangement in a polymer aggregate.⁵⁹ The chain rearrangement and fibril growth after the titration are first characterized by the formation of precursor nanoparticles at an early assembly time point. Figure 3 shows the initial stage of the assembly in mixed solvent, taken immediately after the sample preparation, where nanoparticle aggregates with diameters of 10-14 nm were formed. The cryo-TEM image indicates that these

nanoparticles behaved closely to soft patchy particles that were attracted to each other by hydrophobic interaction. Furthermore, the location of these particles near the hydrophobic lacey carbon structure of the support grids is another indication that they were sticky to the carbon film with hydrophobic patches. The precursor nanoparticles were slowly consumed over several days, as illustrated in the Figure 3 progression, where mixed precursor particles and ill-defined fibril structures with local troughs further support a fusion-like mechanism for fibril growth. The size distribution of initial precursor particles explains the slight inhomogeneity of fibril widths along the length of a fibril and also the roughness of fibril surfaces. The TEM images in Figure 3 do not show the exact 3D shape of the precursor nanoparticles, but given the thin ribbon-like quality of fully formed fibrils, a loosely packed hamburger bun-like geometry with irregularly exposed backbone patches is hypothesized. The exact length of these fibrils is hard to determine as the dimension is much greater than the TEM field of view where we can distinguish individual fibrils.

The rationale for this fibril formation is the semiflexible PGC backbone conformation and the hydrophobicity of the backbone chains, and we expect that the change in solvent quality initiates fibril growth through precursor nanoparticle fusion. To understand how the PGC polymer chains pack in an assembled nanostructure, the effects of both backbone stiffness and hydrophobicity need to be discussed. First, the particular PGC chemistry exhibits significant rigidity due to the inherent stiffness and bulkiness of cyclic glucose monomers that limit conformational freedom, compared to the more commonly known vinyl-based polymers. 60 The persistence length (L_p) of neutral glucose-based polymers is known to range from several to tens of nanometers, 61 and with charged and hydrophobic side chains of each PGC block, the electrostatic and steric repulsions are likely to further enhance the local chain stiffness. Second, during the PGC synthesis, all hydroxyl sites present in glucose are used for installation of side chain moieties or backbone linkages that lead to an overall hydrophobic sugar backbone. In fact, the hydrophilicity of PGC(EEC)₉₈-b-PGC(EPC)(NH₃Cl)₃₀ arises only from one side chain moiety that presents two charged sites displayed from each repeat unit along the hydrophilic block segment. In a solvent that is poor for both the backbone and hydrophobic block, the final nanostructure will require incorporation of all solvophobic components within the core region. Several computational and experimental studies have illustrated such packing of rigid polymers in a non-compatible solvent environment forming a cylindrical nanostructure where the backbone alignment is parallel to the primary axis of the cylinder as opposed to a perpendicular alignment seen in most of the conventional cylindrical micelles. 62,63 The backbone rigidity also forces an interchain parallel alignment of the hydrophobic blocks in the core. Although it is difficult to prove the exact chain configurations and packing of PGCs in the final fibrils, possible mechanisms are proposed after a close examination of the intermediate nanoparticle structure. As shown in Figure 3, the fibril formation is first initiated by the formation of patchy precursors that eventually attach unidirectionally to form long fibrils. The synthesis of soft patchy particles 64,65 and examples of their sequential aggregation into hierarchical structures have been reported previously.⁶⁶ While these previous studies mostly relied on having two or more BCPs mixed within nanoparticles with immiscible blocks forced to locally phase separate and create multidomain, patchy particles, the

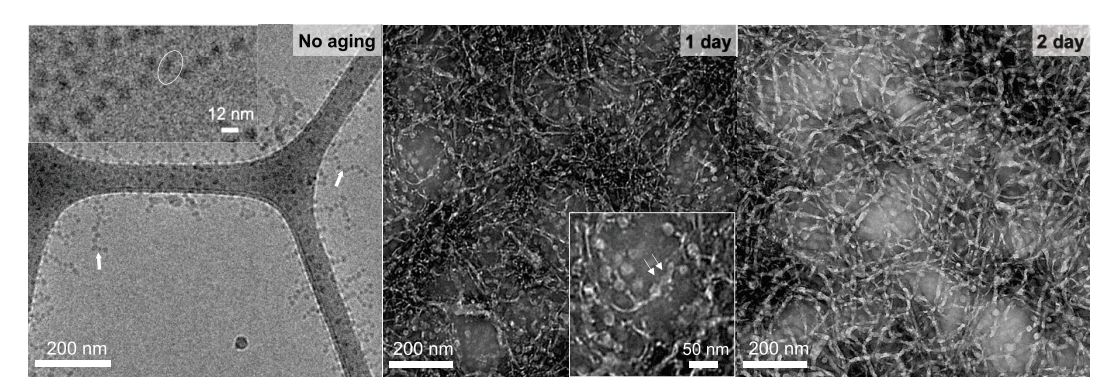


Figure 3. Cryo-TEM image of early assembly stage (no aging) shown on the far left where individual precursors of 10–14 nm diameters are formed. White arrows here highlight the particles in different orientations. With 1 day of aging, a regular TEM image of the intermediate stage shows mixed precursors and loosely formed fibril structures with irregular surfaces. The inset shows a high magnification image of an early stage fibril with troughs showing fusion-like growth. With longer aging, the precursors disappear and more mature regular fibrils form (2 day). All regular TEM images are negatively stained for better contrast. A negatively stained TEM image of the precursors is provided in Figure S4.

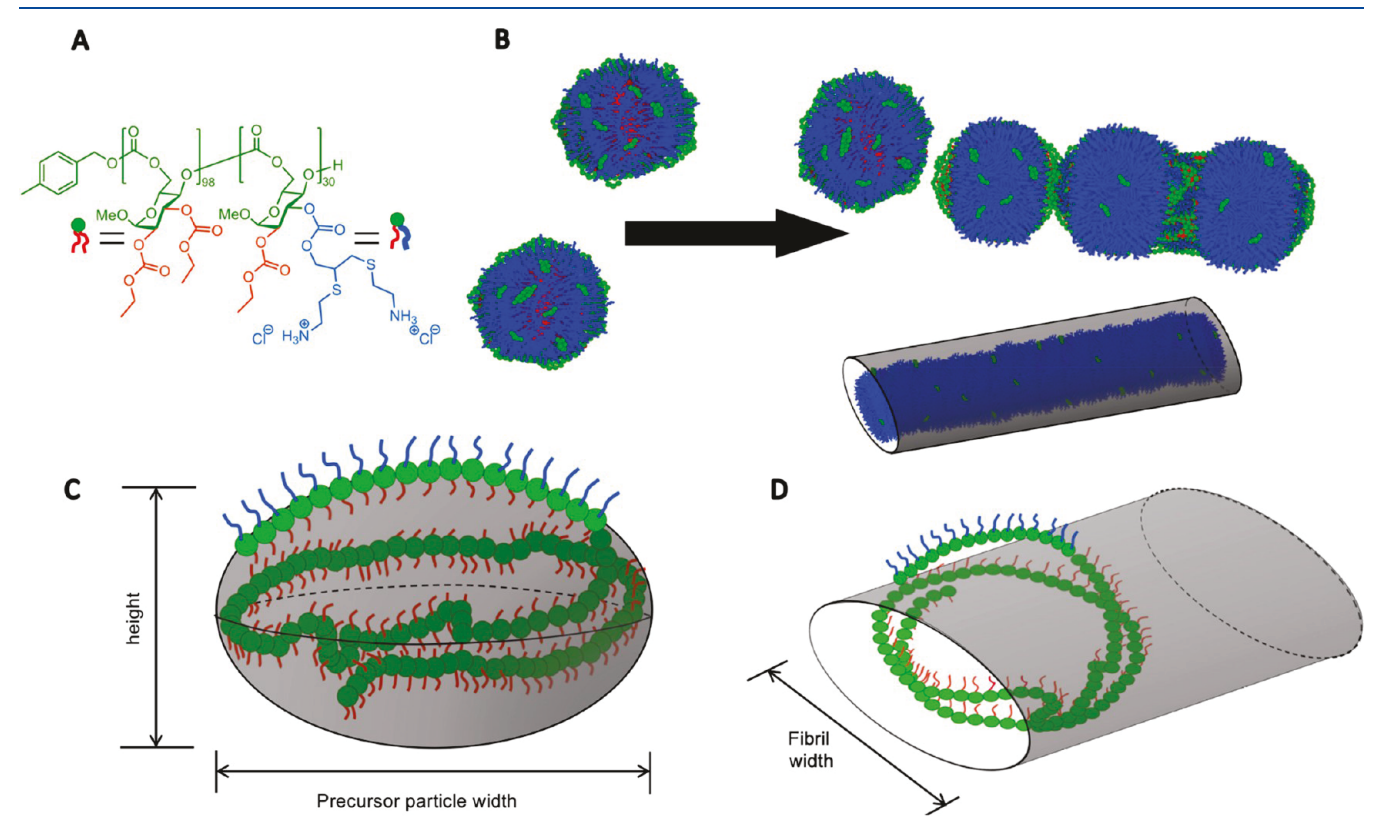


Figure 4. (A) PGC chain schematics shown with the backbone chains in green, charged side chains in blue, and hydrophobic side chains in red. (B) Schematics of initial patchy precursors and their growth mechanism. This is a 2D projection of the particles as viewed from the top, similar to the TEM image. The green hydrophobic patches randomly appear throughout the particles. When patches of two particles approach and interact, the side chains rearrange to reveal a second patch across the particle from the first interparticle interaction. (C) Schematic highlighting an individual chain in a patchy precursor in a side-view cross section. The elliptical cross section is proposed to have PGC chains packed in a toroidal-like configuration to maximize hydrophilic side chain contact with the solvent environment while shielding the backbone in the core. (D) Schematic showing the chain packing after the fibril formation.

proposed mechanism here for the patchy fibril precursors is the local segregation of the PGC backbone and charged side chains in the hydrophilic block. Figure 4A shows the color scheme used for each BCP component, and Figure 4B shows the schematics of the PGC chain packing of the initial aggregate. The PGC backbone (green) and its two hydrophobic ethyl carbonate side chains (red) along the hydrophobic block segment are mostly shielded in the core, whereas the nanoparticle shell displays a more heterogeneous structure

due to collapsed backbone (green) repeat units together with one hydrophobic ethyl carbonate (red) side chain group, complicating the overall hydrophilic effect originating from the charged side chains (blue). This hypothesized chain packing suggests a few important characteristics of PGC BCP assembly: (1) amphiphilic polyelectrolyte-like behavior of the hydrophilic block leads to the phase-segregated hydrophilic block, (2) the unusual PGC backbone chain conformation in an unfavorable solvent condition results in a chain packing different from a

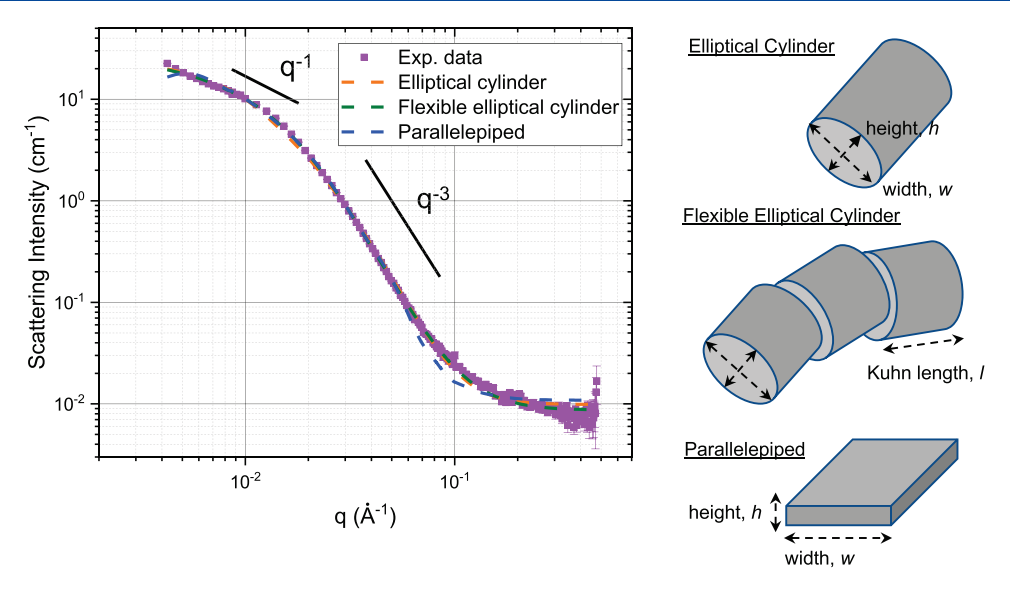


Figure 5. SANS results of PGC fibrils of 0.4 wt % concentration assembled in deuterated solvents. Closed symbols (pink) are experimental data with standard error, and fits are shown in dashed lines with different color schemes for each model used. Fits with polydisperse systems are shown with dashed lines with corresponding colors of the specific models.

conventional core—shell micelle packing, and lastly, (3) the final water volume or the solvent quality helps achieve anisotropic fibril growth.

First, the amphiphilic polyelectrolyte-like behavior of the hydrophilic block is supported by our previous study that observed that the same PGC BCPs assembled into spherical particles in 100% water⁵³ (Figure S5). It was shown that the length of the corona blocks and the intermicellar spacing of the formed particles were both observed and simulated to be extremely short at just several nanometers.⁵³ The results suggested that the corona may have only consisted of charged side chains, while the backbone was likely to be situated near the surface of the denser hydrophobic core aligned perpendicular to the radial direction. The nanoparticle precursors, herein, are expected to have a similar chain packing with the hydrophilic block backbone and its hydrophobic side chain situated close to the core surface and the charged side chains extending out into the solvent as coronal moieties (Figure 4C). This complex hydrophobic-hydrophilic polyelectrolyte behavior of the overall hydrophilic block supports how the patchiness can be created by the proximity of the hydrophobic and hydrophilic parts of the hydrophilic block segment, creating a chain arrangement that maximizes hydrophilic side chain contact with the solvent environment while shielding the PGC backbone and hydrophobic side chain next to the hydrophobic core as shown from the schematics (Figure 4B,C). Second, the semiflexible PGC backbone chains significantly influence the initial aggregate formation and structure. From the cryo-TEM images in Figure 3, the precursor nanoparticle formation is characterized by ill-defined boundaries and inhomogeneous shapes and sizes due to the particle patchiness and organic solvent content swelling the particles. We hypothesize that the PGC backbone chains collapse and wrap around themselves similar to the folding transition of semiflexible chains in a poor solvent (Figure 4C). Sakaue et al. have illustrated a similar phenomenon where a disk-like structure is formed from semiflexible polymers wrapping around themselves to form a toroid. However, with a sufficiently long polymer chain length, the thickness of the torus increased, shrinking the center cavity to form a fat

disk.^{27,28} In the case of the precursor particles herein, the hypothesized polymer chain packing is illustrated in Figure 4C showing the elliptical cross section of the side view. The PGC backbone near the core surface has more orientational ordering to maximize hydrophilic side chain contact and minimize hydrophobic side chain contact with the solvent environment and ensure proper shielding of the hydrophobic, stiff backbones by taking a toroidal-like chain conformation. The particle core is likely occupied by slightly less ordered hydrophobic side chains as well as the PGC backbone. The particular assembly condition with significant organic solvent volume may lead to partially folded PGC chains mixed with tightly packed chains and less ordered chains, similar to a core-shell-type condensed conformation observed with DNA in a moderately poor solvent environment⁶⁷ or a relatively long semiflexible chain.²⁸ Similar to the chain packing in precursor nanoparticles, in fibrils, the hydrophilic block chains are expected to align parallel to the surface, while hydrophobic block chains are partially folded in the core (Figure 4D). The mixed chain folding explains the slight size inconsistency and lack of clear boundaries in TEM images (Figure 3, no aging) shown from the precursor nanoparticles as well as in the final fibrils. Lastly, the THF/water ratio is another important factor that determines the overall fibril formation because it affects the extent of ion pairing vs. ion solvation along the hydrophilic side chains. Patchy precursor nanoparticles allow anisotropic growth of the fibrils where the hydrophobic PGC backbone chains are more easily exposed due to the partial collapsing of corona chains (vide supra). As the proposed packing schematic in Figure 4B shows, the weakly charged side chains that are not able to fully ionize at a low water content do not fully swell and are believed to be collapsed in the center of the precursor exposing the backbone patches. A predominant 1D fusion of precursors is also enhanced by two patchy particles approaching near each other and a significant corona rearrangement, after the first interparticle interaction reveals a second patch across the particle. This process restricts the appearance of multiple patchy sites for branch-like attachment as corona chains reconfigure themselves to avoid crowding. Overall, a moderately poor solvent environment leading to

Table 1. Tabulated Results for Both TEM Data and SANS Model Fitting

results	elliptical cylinder model ^a	flexible elliptical cylinder model ^a	parallelepiped model ^a	cryo-TEM ^b	$TEM^{oldsymbol{b}}$
fibril width, w (nm)	17.2 ± 1.5	15.6 ± 0.6	15.0 ± 4.3	13.2 ± 0.3	14.2 ± 0.5
fibril height, h (nm)	4.0 ± 0.6	3.6 ± 0.5	2.7 ± 0.3	n/a	n/a
Kuhn length (nm)	n/a	5.6 ± 0.5	n/a	n/a	n/a

^aSANS-fitted fibril width and fibril height with standard deviation calculated from the Schulz distribution. Kuhn length is only fitted for the flexible model. ^bAverage and standard deviation of measured fibril widths from cryo-TEM and TEM image analysis.

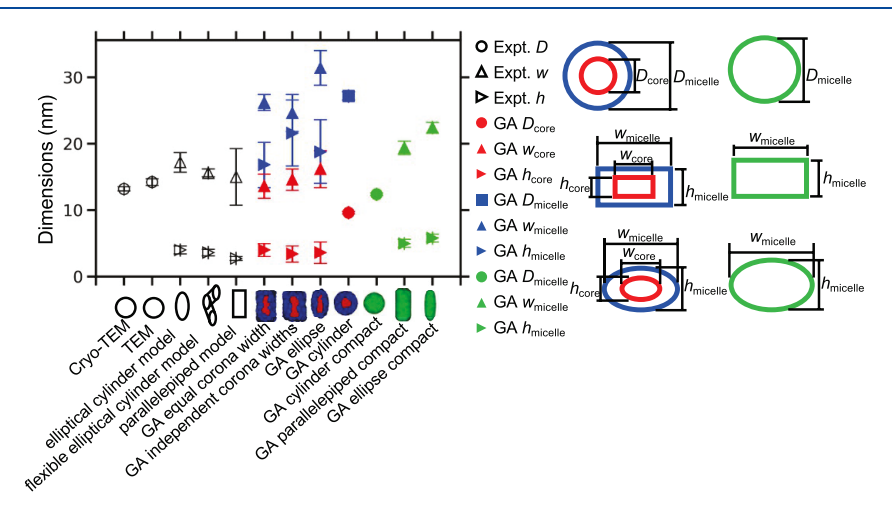


Figure 6. Results for dimensions obtained with TEM, SANS data fit with models in SasView, and SANS data analyzed using the GA part of CREASE for fibrils formed at 0.4 wt %.

both charged side chains and PGC backbone collapse is the most important factor that drives the formation of a patchy precursor and a unidirectional fusion to a long 1D structure.

Additional structural details of PGC fibrils were investigated by SANS experiments. The SANS fibril samples were prepared in mixed deuterated d_8 -THF/D₂O (60/40 v/v %) with the same titration assembly method as above. Figure 5 shows the scattering intensity plotted as a function of scattering vector, q, for PGC fibrils assembled in 0.4 wt % concentration. Figure S6 provides SANS results for a concentration range of 0.04-0.4 wt % showing the presence of fibrils for all concentrations used. The results were initially fitted with models describing an elliptical (elliptical cylinder or flexible elliptical cylinder model) or rectangular (parallelepiped model) cross section with the reported fitting parameters including the fibril height, h, fibril width, w, and Kuhn length of the fibril, l, for the flexible elliptical model. The schematics of each model are included in Figure 5. All SANS data show similar features with q^{-1} behavior in the low q region ranging from 0.04 to 0.01 ${\rm \AA}^{-1}$ suggesting a 1D structure at larger length scales. The initial fitting results are shown in Figure S7 with monodisperse fit parameters. All models fit the data well at low to mid q, demonstrating that all three models are able to capture the longer dimension of the fibril as well as the transition into the scattering of the local fibril structure. While q^{-1} behavior at low q is consistent with the 1D-like fibril structure at longer length scales, the q^{-3} behavior at mid to high q deviates from the typical q^{-4} scattering dependence of nanostructures with sharp interfaces between the nanostructure surface and the surrounding solvent. 68,69 This deviation is thought to result from the roughness and patchiness at the solvent-nanostructure interface characterized by the inhomogeneous fibril surfaces shown from the TEM data and described in Figure 4. The Schulz distribution was then used in the SANS fitting to

account for nanostructure dispersity, which produced significantly better fits than the monodisperse models, especially for the elliptical model fit. Figure 5 shows fittings with polydispersity in dashed lines. The fit results with the Schulz distribution for a fibril height of ~4 nm with a width of ~15 nm are consistent with the microscopy data (Figure 2). Tabulated values for fitted parameters for all models are included in Table 1, and the Schultz distribution values and calculations are presented in Table S1. Although the average fitted fibril dimensions are within the standard deviation between all three models, the flexible elliptical cylinder model provides the best fit with the lowest sse value (Figure S8), suggesting that the cross section of the fibril is likely to resemble an ellipse, consistent with a hamburger bun-like precursor particle geometry.

To go beyond model-based scattering interpretation, the SANS data were also analyzed using the GA part of the CREASE algorithm for a broad range of shapes and two types of BCP packings-typical core-corona arrangements in micelles and a compact PGC BCP packing similar to the proposed packing in Figure 4. For the typical core-corona arrangement, the backbone of the hydrophilic block is considered as part of the corona that extends into the solvent and results in a corona of ~5 nm width from the GA corecorona results. If the typical core-corona arrangement was indeed the case, this corona width would be visible in the cryo-TEM observations as a region around the core of assembled structure. In the compact arrangement, only the hydrophilic side chain decorates the fibril surfaces and would not be clearly distinguishable from the core in TEM images due to their small size and the polydispersity in the fibril dimensions shown in Table 1. Based on these observations, the GA results for the core—corona arrangement do not make physical sense with the dimensions obtained from TEM despite the low sse values of

some of the core-corona arrangement GA results. The disagreement between the TEM measurements and the core-corona-based shape dimensions obtained from GA (Figure 6) supports our hypothesis that the PGC BCPs do not pack in the typical core—corona arrangement; specifically, only the core dimensions for the core-corona shapes match the dimensions obtained from TEM. The best agreement between the dimensions obtained from the GA and those from TEM and SANS fit to the models in SasView is seen for the compact parallelepiped in Figure 6. The next best agreement between the dimensions from the GA and those from the TEM and SANS fit to the models in SasView is seen for the compact ellipse in Figure 6, which maintains an aspect ratio for the cross-sectional dimensions (height and width) similar to the compact parallelepiped. Even though the dimensions obtained with the GA cylinder shape also closely match the dimensions obtained from TEM in Figure 6, the high sse of the GA best structure's $I_{\text{comp}}(q)$ for the compact cylinder, Figure S8, indicates that the $I_{\text{comp}}(q)$ does not match the $I_{\text{exp}}(q)$ as well as the compact parallelepiped and compact elliptical shapes do. This supports the hypothesis that the cross section of the fibril is more elliptical rather than a circle (as in a cylinder). The dimensions and sse obtained from the SANS experiment at 0.04 wt %, shown in Figures S8 and S9, further confirm the dimensions shown in Figure 6 from cryo-TEM, TEM, and SANS models fitted to the data with SasView as well as SANS GA analysis. The GA fitting results are shown in Figure S10.

The SANS data of Figure 7 collected from a series of aging experiments also support the fibril formation progression

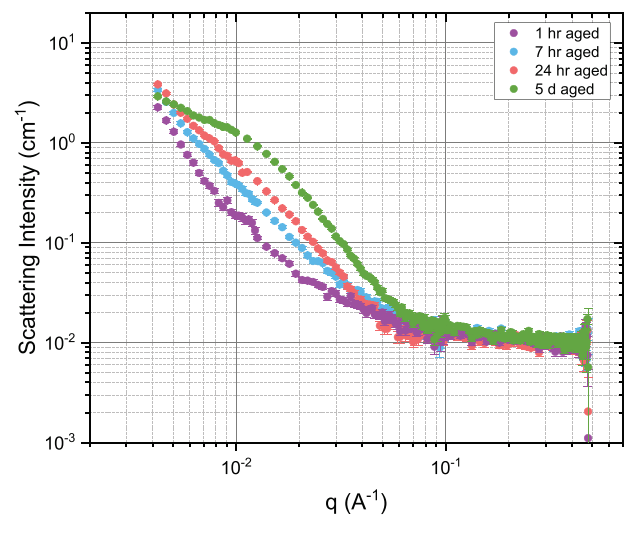


Figure 7. SANS results of PGC fibrils of 0.04 wt % in an aging series from 1 h to 5 days showing an increase in scattering intensity at the mid q region and a shoulder appearance at q = 0.015 Å with aging.

shown by the TEM images in Figure 3. Although a lower concentration at 0.04 wt % was used, the concentration used in the experiment did not affect the fibril formation as confirmed from Figure S6 showing the SANS series of PGC BCPs assembled in different concentrations. The SANS data above show, qualitatively, an increase in the scattering intensity in the low-to-mid q region from 1 h to 5 days of aging indicating formation of larger 1D nanostructures. A consistent upturn at low q at all times shows that the longer dimension of formed nanostructures exceeds the probed length scale of the instrument, even with the least aging possible. This character-

istic illustrates that the patchy particle fusion began to occur at an early assembly stage and that SANS was unable to capture the individual precursor particle structure formation. The data points at 1 h describe rather ill-defined aggregates forming a loosely packed long 1D structure. The progression of scattering profiles with time clearly confirms eventual fibril formation on a similar aging timescale as shown in the microscopy data.

4. CONCLUSIONS

We present here the formation of ribbon-like fibrils from PGCbased amphiphilic BCPs, a biodegradable, natural source-based chemistry. The unique PGC chemistry with a semiflexible hydrophobic backbone that presents two hydrophobic side chains in one block and a combination of one hydrophobic and one hydrophilic side chain in the second block results in an overall amphiphilic character that includes locally amphiphilic polyelectrolyte-like behavior even within the hydrophilic block. Such complexity of local molecular structure then leads to interesting complexity in global solution-state assembly, involving the formation of patchy precursor nanoparticles in which the exposed hydrophobic PGC backbone and side chains provide sticky patchiness in the formed structure. The hydrophobic interparticle association leads to uniform 1D growth of these patchy precursors to a final fibril morphology. The microscopy and scattering data both confirm the formation of fibrillar structures with aging. Although SANS cannot sufficiently capture the characterization of early assembly precursor formation due to its long measurement time, the trend in increased scattering intensity in the mid q region matches well with the fibril growth trend shown from the microscopy data. The illustrated polymer packing schemes of the fibril precursors and the SANS fit with models from SasView and analyzed using the genetic algorithm in CREASE suggest an elliptical cross section of the fibril. Furthermore, due to the slight inhomogeneity of the precursor nanoparticle sizes, the fibril surfaces are characterized by rough, uneven surfaces that are accounted for by using polydisperse models with SANS data fitting. Future work on the PGC BCP assembly includes exploring various solvent conditions to observe the effects of initial solvent quality as well as the final solvent compositions on the overall assembled morphologies. Our results demonstrate that the BCP systems with unconventional chemistries can shed light on the effects of polymer backbone stiffness and hydrophobicity on the BCP solution assembly behavior.

ASSOCIATED CONTENT

Supporting Information

The Supporting Information is available free of charge at https://pubs.acs.org/doi/10.1021/acs.macromol.0c01575.

Description of the genetic algorithm (GA) part of CREASE; cryogenic-TEM image of cationic-modified PGC BCPs in THF; negative stained TEM image of patchy precursor nanoparticles; negative stained TEM image of cationic-modified PGC BCPs assembled in 100% H₂O; small-angle neutron scattering of PGC BCP fibrils in concentration series; small-angle neutron scattering SasView model fitting with monodisperse models; tabulated Schultz distribution; sum of squared errors from GA analysis; fibril dimensions with TEM, SasView SANS model fitting and GA SANS fitting;

complete small-angle neutron scattering fitting using GA (PDF)

AUTHOR INFORMATION

Corresponding Authors

Arthi Jayaraman — Department of Materials Science and Engineering and Department of Chemical and Biomolecular Engineering, University of Delaware, Newark, Delaware 19716, United States; orcid.org/0000-0002-5295-4581; Email: arthij@udel.edu

Karen L. Wooley — Departments of Chemistry, Chemical Engineering, and Materials Science & Engineering, Texas A&M University, College Station, Texas 77842, United States; Email: wooley@chem.tamu.edu

Darrin J. Pochan — Department of Materials Science and Engineering, University of Delaware, Newark, Delaware 19716, United States; Email: pochan@udel.edu

Authors

Jee Young Lee — Department of Materials Science and Engineering, University of Delaware, Newark, Delaware 19716, United States; orcid.org/0000-0002-5259-3659

Yue Song — Departments of Chemistry, Chemical Engineering, and Materials Science & Engineering, Texas A&M University, College Station, Texas 77842, United States; ⊚ orcid.org/0000-0002-7800-5528

Michiel G. Wessels – Department of Chemical and Biomolecular Engineering, University of Delaware, Newark, Delaware 19716, United States

Complete contact information is available at: https://pubs.acs.org/10.1021/acs.macromol.0c01575

Notes

The authors declare no competing financial interest.

■ ACKNOWLEDGMENTS

We acknowledge the financial support from the National Science Foundation under grant numbers NSF DMREF-1629156 and DMREF-1629094 and the Welch Foundation through the W. T. Doherty Welch Chair in Chemistry (KLW, A-0001). Access to an NGB-30m SANS instrument was provided by the Center for High Resolution Neutron Scattering, a partnership between the National Institute of Standards and Technology and the National Science Foundation under agreement no. DMR-1508249. Beam time was available through the UD-NIST Center for Neutron Science under cooperative agreements 70NANB12H239 and 370NANB17H302 from the NIST, U.S. Department of Commerce. Neutron facilities are also supported in part by the National Science Foundation under agreement no. DMR-0944772. This work benefited from the use of the SasView application, originally developed under NSF award DMR-0520547. SasView contains code developed with funding from the European Union's Horizon 2020 Research and Innovation Programme under the SINE2020 project, grant agreement no. 654000. Support is also acknowledged from the Keck Center for Advanced Microscopy and Microanalysis. We also acknowledge the support for the genetic algorithm work through the use of the Information Technologies resources at the University of Delaware, specifically the Farber highperformance computing resources.

REFERENCES

- (1) Jain, S.; Bates, F. S. Consequences of Nonergodicity in Aqueous Binary PEO-PB Micellar Dispersions. *Macromolecules* **2004**, 37, 1511–1523
- (2) Zhang, L.; Eisenberg, A. Multiple Morphologies and Characteristics of "Crew-Cut" Micelle-like Aggregates of Polystyrene- b-Poly(Acrylic Acid) Diblock Copolymers in Aqueous Solutions. J. Am. Chem. Soc. 1996, 118, 3168—3181.
- (3) Greenall, M. J.; Schuetz, P.; Furzeland, S.; Atkins, D.; Buzza, D. M. A.; Butler, M. F.; McLeish, T. C. B. Controlling the Self-Assembly of Binary Copolymer Mixtures in Solution through Molecular Architecture. *Macromolecules* **2011**, *44*, 5510–5519.
- (4) Petkau-Milroy, K.; Ianiro, A.; Ahn, M. M. L.; Magana, J. R.; Vleugels, M. E. J.; Lamers, B. A. G.; Tuinier, R.; Voets, I. K.; Palmans, A. R. A.; Meijer, E. W. Architecture-Dependent Interplay between Self-Assembly and Crystallization in Discrete Block Co-Oligomers. *ACS Macro Lett.* **2020**, *9*, 38–42.
- (5) Ohnsorg, M. L.; Ting, J. M.; Jones, S. D.; Jung, S.; Bates, F. S.; Reineke, T. M. Tuning PNIPAm Self-Assembly and Thermoresponse: Roles of Hydrophobic End-Groups and Hydrophilic Comonomer. *Polym. Chem.* **2019**, *10*, 3469–3479.
- (6) Wang, X.; An, Z. New Insights into RAFT Dispersion Polymerization-Induced Self-Assembly: From Monomer Library, Morphological Control, and Stability to Driving Forces. *Macromol. Rapid Commun.* **2019**, 40, 1–14.
- (7) Wang, E.; Zhu, J.; Zhao, D.; Xie, S.; Bates, F. S.; Lodge, T. P. Effect of Solvent Selectivity on Chain Exchange Kinetics in Block Copolymer Micelles. *Macromol. Symp.* **2020**, *53*, 417–426.
- (8) Pietsch, C.; Mansfeld, U.; Guerrero-Sanchez, C.; Hoeppener, S.; Vollrath, A.; Wagner, M.; Hoogenboom, R.; Saubern, S.; Thang, S. H.; Remzi Becer, C.; et al. Thermo-Induced Self-Assembly of Responsive Poly(DMAEMA-b-DEGMA) Block Copolymers into Multi-and Unilamellar Vesicles. *Macromolecules* 2012, 45, 9292–9302.
- (9) Zhang, L.; Yu, K.; Eisenberg, A. Ion-Induced Morphological Changes in "Crew-Cut" Aggregates of Amphiphilic Block. *Science* **1996**, 272, 1777–1779.
- (10) Cui, H.; Chen, Z.; Zhong, S.; Wooley, K. L.; Pochan, D. J. Block Copolymer Assembly via Kinetic Control. *Science* **2007**, 317, 647–650.
- (11) Gao, Y.; Qiu, H.; Zhou, H.; Li, X.; Harniman, R.; Winnik, M. A.; Manners, I. Crystallization-Driven Solution Self-Assembly of Block Copolymers with a Photocleavable Junction. *J. Am. Chem. Soc.* **2015**, 137, 2203–2206.
- (12) Chen, Y.; Zhang, K.; Wang, X.; Zhang, F.; Zhu, J.; Mays, J. W.; Wooley, K. L.; Pochan, D. J. Multigeometry Nanoparticles: Hybrid Vesicle/Cylinder Nanoparticles Constructed with Block Copolymer Solution Assembly and Kinetic Control. *Macromolecules* **2015**, *48*, 5621–5631.
- (13) Wyman, I.; Njikang, G.; Liu, G. When Emulsification Meets Self-Assembly: The Role of Emulsification in Directing Block Copolymer Assembly. *Prog. Polym. Sci.* **2011**, *36*, 1152–1183.
- (14) Shin, J. J.; Kim, E. J.; Ku, K. H.; Lee, Y. J.; Hawker, C. J.; Kim, B. J. 100th Anniversary of Macromolecular Science Viewpoint: Block Copolymer Particles: Tuning Shape, Interfaces, and Morphology. *ACS Macro Lett.* **2020**, *9*, 306–317.
- (15) Varlas, S.; Foster, J. C.; Arkinstall, L. A.; Jones, J. R.; Keogh, R.; Mathers, R. T.; O'reilly, R. K. Predicting Monomers for Use in Aqueous Ring-Opening Metathesis Polymerization-Induced Self-Assembly. ACS Macro Lett. 2019, 8, 466–472.
- (16) Kuwajima, K.; Goto, Y.; Hirata, F.; Kataoka, M.; Terazima, M. Water and Biomolecules: Physical Chemistry of LIfe Phenomena; Biological and Medical Physics, Biomedical Engineering; Springer: Berlin, 2009.
- (17) Buhler, E.; Boué, F. Persistence Length for a Model Semirigid Polyelectrolyte as Seen by Small Angle Neutron Scattering: A Relevant Variation of the Lower Bound with Ionic Strength. *Eur. Phys. J. E* **2003**, *10*, 89–92.
- (18) Pereira, G. G. Charged, Semi-Flexible Polymers under Incompatible Solvent Conditions. *Curr. Appl. Phys.* **2008**, *8*, 347–350.

- (19) Leforestier, A. Polymorphism of DNA Conformation inside the Bacteriophage Capsid. *J. Biol. Phys.* **2013**, *39*, 201–213.
- (20) Shi, B.; Zheng, M.; Tao, W.; Chung, R.; Jin, D.; Ghaffari, D.; Farokhzad, O. C. Challenges in DNA Delivery and Recent Advances in Multifunctional Polymeric DNA Delivery Systems. *Biomacromolecules* **2017**, *18*, 2231–2246.
- (21) Tan, Z.; Jiang, Y.; Zhang, W.; Karls, L.; Lodge, T. P.; Reineke, T. M. Polycation Architecture and Assembly Direct Successful Gene Delivery: Micelleplexes Outperform Polyplexes via Optimal DNA Packaging. *J. Am. Chem. Soc.* **2019**, *141*, 15804–15817.
- (22) Montesi, A.; Pasquali, M.; Mackintosh, F. C. Collapse of a Semiflexible Polymer in Poor Solvent. *Phys. Rev. E* **2004**, *69*, No. 021916.
- (23) Gosule, L. C.; Schellman, J. A. Compact Form of DNA Induced by Spermidine. *Nature* **1976**, 259, 333–335.
- (24) Shen, M. R.; Downing, K. H.; Balhorn, R.; Hud, N. V. Nucleation of DNA Condensation by Static Loops: Formation of DNA Toroids with Reduced Dimensions. *J. Am. Chem. Soc.* **2000**, 122, 4833–4834.
- (25) Sakaue, T.; Yoshikawa, K. Folding/Unfolding Kinetics on a Semiflexible Polymer Chain. J. Chem. Phys. 2002, 117, 6323–6330.
- (26) Miller, I. C. B.; Keentok, M.; Pereira, G. G.; Williams, D. R. M. Semiflexible Polymer Condensates in Poor Solvents: Toroid versus Spherical Geometries. *Phys. Rev. E* **2005**, *71*, No. 031802.
- (27) Sakaue, T. Emergence of Multiple Tori Structures in a Single Polyelectrolyte Chain. J. Chem. Phys. 2004, 120, 6299–6305.
- (28) Higuchi, Y.; Sakaue, T.; Yoshikawa, K. Chain Length Dependence of Folding Transition in a Semiflexible Homo-Polymer Chain: Appearance of a Core-Shell Structure. *Chem. Phys. Lett.* **2008**, 461, 42–46.
- (29) Werlich, B.; Taylor, M.; Shakirov, T.; Paul, W. On the Pseudo Phase Diagram of Single Semi-Flexible Polymer Chains: A Flat-Histogrammonte Carlo Study. *Polymer* **2017**, *9*, 38.
- (30) Dey, A.; Reddy, G. Toroidal Condensates by Semiflexible Polymer Chains: Insights into Nucleation, Growth and Packing Defects. *J. Phys. Chem. B* **2017**, *121*, 9291–9301.
- (31) Li, X.; Bates, F. S.; Dorfman, K. D. Rapid Conformational Fluctuations in a Model of Methylcellulose. *Phys. Rev. Mater.* **2017**, *1*, 25604.
- (32) Huang, W.; Ramesh, R.; Jha, P. K.; Larson, R. G. A Systematic Coarse-Grained Model for Methylcellulose Polymers: Spontaneous Ring Formation at Elevated Temperature. *Macromolecules* **2016**, *49*, 1490–1503.
- (33) Lott, J. R.; Mcallister, J. W.; Wasbrough, M.; Sammler, R. L.; Bates, F. S.; Lodge, T. P. Fibrillar Structure in Aqueous Methylcellulose Solutions and Gels. *Macromolecules* **2013**, *46*, 9760–9771.
- (34) Ginzburg, V. V.; Sammler, R. L.; Huang, W.; Larson, R. G. Anisotropic Self-Assembly and Gelation in Aqueous Methylcellulose—Theory and Modeling. *J. Polym. Sci. Part B Polym. Phys.* **2016**, *54*, 1624–1636.
- (35) Liu, W.; Liu, Y.; Hao, X.; Zeng, G.; Wang, W.; Liu, R.; Huang, Y. Backbone-Collapsed Intra- and Inter-Molecular Self-Assembly of Cellulose-Based Dense Graft Copolymer. *Carbohydr. Polym.* **2012**, *88*, 290–298.
- (36) Liu, W.; Liu, R.; Li, Y.; Kang, H.; Shen, D.; Wu, M.; Huang, Y. Self-Assembly of Ethyl Cellulose-Graft-Polystyrene Copolymers in Acetone. *Polymer* **2009**, *50*, 211–217.
- (37) Olsen, B. D.; Segalman, R. A. Self-Assembly of Rod-Coil Block Copolymers. *Mater. Sci. Eng. R Rep.* **2008**, *62*, 37–66.
- (38) Xu, F.; Zhang, J.; Zhang, P.; Luan, X.; Mai, Y. "Rod-Coil" Copolymers Get Self-Assembled in Solution. *Mater. Chem. Front.* **2019**, *3*, 2283–2307.
- (39) Tao, Y.; Ma, B.; Segalman, R. A. Self-Assembly of Rod-Coil Block Copolymers and Their Application in Electroluminescent Devices. *Macromolecules* **2008**, *41*, 7152–7159.
- (40) Mori, T.; Watanabe, T.; Minagawa, K.; Tanaka, M. Self-Assembly of Oligo(*p*-Phenylenevinylene)-*Block*-Poly(Ethylene Oxide) in Polar Media and Solubilization of an Oligo(*p*-Phenylenevinylene)

- Homooligomer inside the Assembly. J. Polym. Sci., Part A: Polym. Chem. 2005, 43, 1569–1578.
- (41) Wang, H.; You, W.; Jiang, P.; Yu, L.; Wang, H. H. Supramolecular Self-Assembly of Conjugated Diblock Copolymers. *Chem. Eur. J.* **2004**, *10*, 986–993.
- (42) Bellomo, E. G.; Wyrsta, M. D.; Pakstis, L.; Pochan, D. J.; Deming, T. J. Stimuli-Responsive Polypeptide Vesicles by Conformation-Specific Assembly. *Nat. Mater.* **2004**, *3*, 244–248.
- (43) Shen, J.; Chen, C.; Fu, W.; Shi, L.; Li, Z. Conformation-Specific Self-Assembly of Thermo-Responsive Poly(Ethylene Glycol)-b-Polypeptide Diblock Copolymer. *Langmuir* **2013**, *29*, 6271–6278.
- (44) Yu, B.; Danielsen, S. P. O.; Patterson, A. L.; Davidson, E. C.; Segalman, R. A. Effects of Helical Chain Shape on Lamellae-Forming Block Copolymer Self-Assembly. *Macromolecules* **2019**, *52*, 2560–2568
- (45) Williams, D. R. M.; Fredrickson, G. H. Cylindrical Micelles in Rigid-Flexible Diblock Copolymers. *Macromolecules* **1992**, *25*, 3561–3568.
- (46) Cooke, I. R.; Williams, D. R. M. Collapse of Flexible-Semiflexible Copolymers in Selective Solvents: Single Chain Rods, Cages, and Networks. *Macromolecules* **2004**, *37*, 5778–5783.
- (47) Zhu, J.; Zhang, S.; Zhang, F.; Wooley, K. L.; Pochan, D. J. Hierarchical Assembly of Complex Block Copolymer Nanoparticles into Multicompartment Superstructures through Tunable Interparticle Associations. *Adv. Funct. Mater.* **2013**, 23, 1767–1773.
- (48) Lunn, D. J.; Gould, O. E. C.; Whittell, G. R.; Armstrong, D. P.; Mineart, K. P.; Winnik, M. A.; Spontak, R. J.; Pringle, P. G.; Manners, I. Microfibres and Macroscopic Films from the Coordination-Driven Hierarchical Self-Assembly of Cylindrical Micelles. *Nat. Commun.* 2016, 7, 12371.
- (49) Srinivas, G.; Pitera, J. W. Soft Patchy Nanoparticles from Solution-Phase Self-Assembly of Binary Diblock Copolymers. *Nano Lett.* **2008**, *8*, 611–618.
- (50) Qiu, H.; Hudson, Z. M.; Winnik, M. A.; Manners, I. Multidimensional Hierarchical Self-Assembly of Amphiphilic Cylindrical Block Comicelles. *Science* **2015**, *347*, 1329–1332.
- (51) Kratz, K.; Breitenkamp, K.; Hule, R.; Pochan, D.; Emrick, T. PC-Polyolefins: Synthesis and Assembly Behavior in Water. *Macromolecules* **2009**, 42, 3227–3229.
- (52) Atanase, L. I.; Desbrieres, J.; Riess, G. Micellization of Synthetic and Polysaccharides-Based Graft Copolymers in Aqueous Media. *Prog. Polym. Sci.* **2017**, *73*, 32–60.
- (53) Beltran-Villegas, D. J.; Wessels, M. G.; Lee, J. Y.; Song, Y.; Wooley, K. L.; Pochan, D. J.; Jayaraman, A. Computational Reverse-Engineering Analysis for Scattering Experiments on Amphiphilic Block Polymer Solutions. *J. Am. Chem. Soc.* **2019**, *141*, 14916–14930.
- (54) Su, L.; Khan, S.; Fan, J.; Lin, Y.-N.; Wang, H.; Gustafson, T. P.; Zhang, F.; Wooley, K. L. Functional Sugar-Based Polymers and Nanostructures Comprised of Degradable Poly(D-Glucose Carbonate)S. *Polym. Chem.* **2017**, *8*, 1699–1707.
- (55) Schindelin, J.; Arganda-Carreras, I.; Frise, E.; Kaynig, V.; Longair, M.; Pietzsch, T.; Preibisch, S.; Rueden, C.; Saalfeld, S.; Schmid, B.; et al. Fiji: An Open-Source Platform for Biological-Image Analysis. *Nat. Methods* **2012**, *9*, 676–682.
- (56) Kline, S. R. Reduction and Analysis of SANS and USANS Data Using IGOR Pro. *J. Appl. Crystallogr.* **2006**, *39*, 895–900.
- (57) Doucet, M.; Cho, J. H.; Alina, G.; Bakker, J.; Bouwman, W.; Butler, P.; Campbell, K.; Gonzales, M.; Heenan, R.; Jackson, A. SasView Version 4.2.2. 2017, DOI: 10.5281/zenodo.2652478.
- (58) Mai, Y.; Eisenberg, A. Self-Assembly of Block Copolymer. Chem. Soc. Rev. 2012, 41, 5969–5985.
- (59) Pochan, D. J.; Zhu, J.; Zhang, K.; Wooley, K. L.; Miesch, C.; Emrick, T. Multicompartment and Multigeometry Nanoparticle Assembly. *Soft Matter* **2011**, *7*, 2500–2506.
- (60) Gidley, M. J.; Nishinari, K. Chemistry, Biochemistry, and Biology of 1–3 Beta Glucans and Related Polysaccharides, 1st ed.; Elsevier/Academic Press: Burlington, MA, 2009.

- (61) Kamide, K.; Saito, M. Persistence Length of Cellulose and Cellulose Derivatives in Solution. *Macromol. Chem. Rapid Commun.* **1983**, *4*, 33–39.
- (62) Kim, K. H.; Huh, J.; Jo, W. H. Wirelike Micelle Formed by a T-Shaped Graft Copolymer with a Rigid Backbone. *Macromolecules* **2004**, *37*, 676–679.
- (63) Jiang, S.; Xia, K.-Q.; Xu, G. Effect of Additives on Self-Assembling Behavior of Nafion in Aqueous Media. *Macromolecules* **2001**, *34*, 7783–7788.
- (64) Gröschel, A. H.; Müller, A. H. E. Self-Assembly Concepts for Multicompartment Nanostructures. *Nanoscale* **2015**, *7*, 11841–11876.
- (65) Wyman, I. W.; Liu, G. Micellar Structures of Linear Triblock Terpolymers: Three Blocks but Many Possibilities. *Polymer* **2013**, *54*, 1950–1978.
- (66) Jo, I. S.; Lee, S.; Zhu, J.; Shim, T. S.; Yi, G. R. Soft Patchy Micelles. Curr. Opin. Colloid Interface Sci. 2017, 30, 97–105.
- (67) Baigl, D.; Yoshikawa, K. Dielectric Control of Counterion-Induced Single-Chain Folding Transition of DNA. *Biophys. J.* **2005**, 88, 3486–3493.
- (68) Sivia, D. S. Elementary Scattering Theory: For Xray And Neutron Users, 1st ed.; Oxford University Press: Oxford, 2011.
- (69) Hammouda, B.; Krueger, S.; Glinka, C. J. Small Angle Neutron Scattering at the National Institute of Standards and Technology. *J. Res. Natl. Inst. Stand. Technol.* **1993**, 98, 46.